ADVANCED MATERIALS TECHNOLOGIES
www.advmattechnol.de

Shape Memory Alloy Thin Film Auxetic Structures

*Duygu Dengiz, Hauke Goldbeck, Sabrina M. Curtis, Lars Bumke, Justin Jetter, and Eckhard Quandt**

Auxetic structures provide an interesting approach to solving engineering problems due to their negative Poisson's ratio, which allows for elongation perpendicular to applied stresses, opposite to a conventional structure's necking behavior. Thus, they can function well in applications requiring compacting the device into a small volume during the deployment (e.g., implants inserted with catheters) or stretchability with area coverage (e.g., stretchable electronics). Fabricating them with shape memory alloys (SMAs) expands the possibilities. The high strains experienced by auxetic structures may become reversible compared to ordinary metals due to superelastic or shape memory effect. This work studies four different auxetic microstructures using thin film SMAs that are capable of surviving strains up to 57.4%. Since these structures are fabricated by layer deposition and lithography, other components, such as microelectronics, can be seamlessly integrated into the fabrication process. These auxetic thin films are investigated for their mechanical behavior under tension for their stretchability and stability. Under tension, thin films are known to show wrinkling instabilities. In two of four designs, the large auxetic behavior leads to wrinkling, while the other two display stable, non-wrinkling behavior. These designs can be candidates for stretchable electronics, wearable medical devices (e.g., biosensors), or implants (e.g., stents).

1. Introduction

Auxetic structures (negative Poisson's ratio) are known for their ability to enhance energy absorption, indentation resistance, shear stress, and fracture toughness.[1] They also display synclastic bending and the ability to adapt to various curvatures.[2] These improvements have led to auxetic structures being investigated for applications such as energy absorbers,[3] blast panels,[4] filters,[5] displays,[6] and implants.[7] In addition to implants, these structures have also been used as thin film polymer scaffolds for cell growth at high strains, providing an interesting insight into the potential biomedical applications possible with these structures.[8] The Poisson's ratio can be adjusted by introducing patterns (porosity). Moreover, the in-plane deformations of these structures remain in the elastic region, the behavior of the modified Poisson's ratio is controlled solely by the geometry and not by the intrinsic properties of the material.[9]

In principle, auxetic structures can be made from all classes of materials, such as polymeric[10–12] ceramic,[13] and metallic materials.[13,14] In the case of metals, shape memory alloys (SMAs) are of particular interest due to the large strains these materials can withstand. They have been investigated as relatively large-format auxetic TiNi antennas[15] 4D printed ballistic panels with TiNi,[16] 4D printed Fe-Mn-Si based SMAs,[17] and auxetic unit cells made of superelastic TiNi-CuCo thin-films for stretchable electronics.[18]

SMAs are generally used in two ways: either by employing the shape memory effect or leveraging superelastic behavior provided by the thermally or stress-induced martensitic phase transformations. In TiNi-based SMA, reversible intrinsic strains up to 8%[19] can be achieved, while using the shape memory effect heating to the high-temperature phase austenite is required to recover the deformation reversibly. The reversible pseudoelastic behavior for superelastic alloys is related to the stress-induced martensitic phase transformation from austenite to martensite. Reversibility, in this case, is achieved by simply removing the applied load. Depending on the application's requirements, an SMA's transformation temperature may be adjusted through heat treatments or composition changes.[20–22] Chluba et al. have shown that the ternary shape memory alloy TiNiCu exhibits no fatigue even after 10 million superelastic cycles,[23] which would make this alloy a good candidate for applications such as skintronics (stretchable electronics applied onto the skin), where a device at the elbows or knees may be subjected to high numbers of cycles and at large strains. Conventional metals such as copper embedded in a polymer were studied for their cycling behavior and showed cracks up to strains of 5%.[24] In applications in the human

D. Dengiz, H. Goldbeck, S. M. Curtis, L. Bumke, J. Jetter, E. Quandt
Faculty of Engineering
Kiel University
24143 Kiel, Germany
E-mail: eq@tf.uni-kiel.de
S. M. Curtis
Department of Materials Science and Engineering
University of Maryland
College Park, MD 20742, USA
The ORCID identification number(s) for the author(s) of this article can be found under https://doi.org/10.1002/admt.202201991.

DOI: 10.1002/admt.202201991

body, biocompatible binary NiTi is a commonly used implant material.[25] TiNiCuCo free-standing serpentine interconnects were demonstrated to reach maximum strains (serpentine elongations) of 156% with low electrical resistivity (5.43×10^{-7} Ω m). TiNiCuCo serpentines were also demonstrated to serve as free-standing substrates for other stretchable conductors.[26]

Thin film structures under tensile stress can show an additional phenomenon besides the corresponding elongation, wrinkling due to buckling. Because the clamped borders prevent lateral shrinkage of the film, which leads to the creation of the compression regions, and with these compressed regions, in-plane strain mismatch is generated by the Poisson's ratio of the material.[27] This results in structural instability due to tensile loading and results in local surface wave formations.[28] Furthermore, Su et al. showed that the thickness–width ratio affects buckling. Below one, they show ultra-thin films wrinkles for samples' thickness smaller than 1 μm, and with increasing the thickness, they reported buckling and scissoring regions. For in-plane deformation the thickness should be higher than the width.[29] These out-of-plain deformations may lead to multiple consequences, such as loss of contact with a surface and/or stress concentration due to shape change. Therefore, wrinkling and its prevention in free-standing self-supporting thin films should be well understood. Understanding and controlling wrinkling may allow for use directly in the body as implants require certain radial forces to prevent implant migration,[30] and auxetics are studied as having high radial forces.[31] Therefore, non-wrinkling auxetics may provide a foundation for highly stable implants.

Although wrinkling is primarily studied in polymer thin films,[32–34] some literature focuses on metallic thin films on polymer substrates[35,36] and patterned free-standing Al thin films as a function of structural parameters. By patterning Al and using different material properties, Flores-Johnson et al. revealed that plasticity significantly affects wrinkling formation and amplitude. They showed that a material's elastic-plastic properties play an important role in wrinkling. They found that purely elastic material displays wrinkling at very high strains compared to the elastic–plastic material model.[37] Using shape memory alloy with high intrinsic recoverable strains gives the potential for high stretchability prior to wrinkling deformations. Adjusting material properties, such as high intrinsic strain superelastic material, high stretchability, and full recovery could be achieved in an auxetic thin film. Bonfanti et al. compared comparatively large polymer thin films where one sample had a negative Poisson's ratio (auxetic) pattern and the other with a positive Poisson's ratio diamond pattern. They found that the wrinkling behavior of the sample with a negative Poisson's ratio changed drastically compared to the one with a positive Poisson's ratio and that the wrinkling occurred at the edges rather than in the center of the film as expected from conventional wrinkling behavior.[38]

MEMS (Microelectromechanical systems) techniques (photolithography, magnetron sputtering, and etching techniques) provide the freedom to implement complex film patterns with different components of microelectronics, as demonstrated by bioelectrodes[39] and sensors.[40,41] In this study, the fabrication and investigation of miniaturized by using MEMS free-standing binary NiTi thin films are the primary focus, with four different auxetic structures adopted from literature to study auxetic and wrinkling behavior. The thickness–width ratio effect tried to be avoided in the individual unit cells of the auxetics, so in this paper, only the macroscopic wrinkling effect is investigated. The experimental results are discussed in comparison with FE simulations to allow fabrication-free investigations of auxetic structures in the future.

2. Experimental Section

Structured free-standing films were fabricated using photolithography, wet chemical etching of sacrificial layer of copper, and magnetron sputtering, described in detail by Bechtold et al.[42] The fabrication quality of the edges can be seen in Figure S1 (Supporting Information). The auxetic structures pattern was transferred to a 4-in. Si Wafer by photolithography (Karl Suss MA6, Germany). Depending on the desired composition and properties (SE or SME), NiTi films with a thickness of around 45 μm were deposited using a Von Ardenne CS730S (Von Ardenne, Germany) cluster magnetron sputter device from a 4-in. $TiNi_{46}$ or $TiNi_{46.5}$ target (Ingpuls GmbH, Germany) with 2×10^{-3} mbar pressure, 20 sccm argon flow, and 150 W resulting in a deposition rate of 3.3 μm h^{-1}. The elemental composition averaged over a 4-in. Si wafer of the as deposited films was measured by Energy dispersive X-Ray spectroscopy (EDS) using a Helios NanoLab 600 scanning electron microscopy (SEM, FEI, Germany) equipped with a silicon drift detector (Oxford Instruments, UK). The composition was determined to $Ti_{49}Ni_{51}$ (SE) and $Ti_{51}Ni_{49}$ (SME) with an error of 0.5 at% using a binary $Ti_{50.4}Ni_{49.6}$ standard. For further experiments, the samples from a radius of 30 mm around the center were used in each case to ensure the consistency of the composition. Amorphous free-standing tensile test structures were heat treated by rapid thermal annealing (RTA, CreaTec RTA-6 SY09, Germany) for superelastic samples at 700 °C for 300 s and 500 °C for 300 s. Shape memory effect samples were treated at 650 °C for 300 s and 500 °C for 300 s, with the first step contributing to material crystallization and the second step precipitation. Mechanical properties were analyzed by tensile testing (Zwick Roell Z.05, Germany) by using 0.5 N pre-load and a speed of 0.12 mm min^{-1} with a simple dog bone structure. The same tensile parameters without pre-load were also employed for the auxetic dog bones. All the experiments were performed at temperature of 26 ± 1 °C to ensure consistent material properties.

The auxetic designs used within this study, shown in **Figure 1**, were adapted from proposed designs from previous studies. Design 1 was based on rotating triangles,[43] and Design 2 was a new type of auxetic with high compressibility called "s-shape auxetics,"[44] which can be advantageous for specific applications such as stents which require high crimpability into a catheter. Design 3 was based on rotating squares and was already used as an implant with laser-cut stainless steel.[7] Design 4 was based on a circular auxetic structure that was used for a piezoelectric energy harvester.[45] Figure 1e shows a general arrangement of an auxetic structured tensile test specimen with a total length of 14 mm and a width of 5 mm. The auxetic structure area was a total of 20 mm^2 with a length of

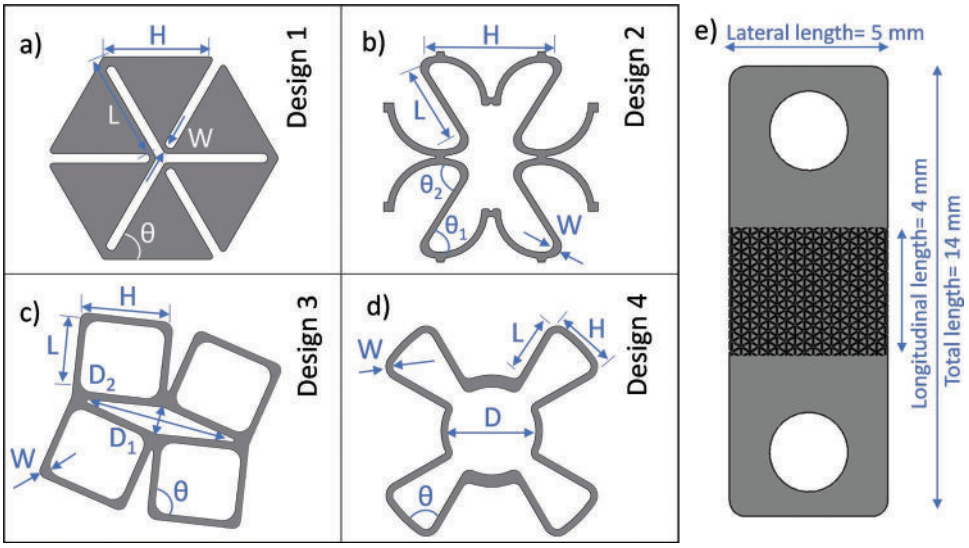

Figure 1. Four different auxetic structures investigated in this study with labeled dimensions: *H* height, *W* width, *L* length, *D* diameter, and *Θ* the angle. a) Rotating triangles, b) s-shape auxetic, c) rotating-squares, d) circular auxetic, e) auxetic tensile dog bone with lateral and longitudinal dimensions of 5 mm × 4 mm at equilibrium, respectively.

4 mm and a width of 5 mm. **Table 1** shows the dimensions of the array designs with *H* height, *W* width, *L* length, *D* diameter, and *Θ* the angle, where the thickness is 45 µm and the width *W* is 35 µm in each case.

Nikon D850 with AF-S micro Nikkor 60 lens was used for the photos and videos of the auxetic dog bones. A setup was made for applying displacement with a micrometer head to the structured dog bones. The data related to Poisson's ratios of the samples were obtained with the photos using Image J (U. S. National Institutes of Health, USA). The Poisson's ratio was defined by the change in lateral strains divided by longitudinal strains. The SEM images were performed on specimens with defined, pre-set strains using Zeiss Ultra 55 Plus (Zeiss, Germany).

Abaqus (Dassault Systemes) was used to simulate the behavior of the tensile structures under certain strains using the built-in superelastic material model for binary TiNi. The superelastic material model properties E_A (Elastic modulus of austinite), E_M (Elastic modulus of martensite), σ^S_{tL} (tensile stress start of loading), σ^E_{tL} (tensile stress start of loading), σ^S_{tU} (tensile stress start of unloading), $\sigma^E_{tU,}$ (tensile stress end of unloading), and ε_L (transformation strain), were obtained from experiments, and ν_A (Poisson's ratio of austinite), ν_M (Poisson's ratio of martensite), σ^S_{cL} (compression stress start of loading), $(\delta\sigma/\delta T)_L$ (Clausius–Clapeyron coefficient loading), $(\delta\sigma/\delta T)_U$ (Clausius–Clapeyron coefficient unloading), and T_o set experimental temperature were implemented from Velvaluri et al. for a binary TiNi thin film.[46] These material parameters can be found in **Table 2**.

For the wrinkling simulation, the Riks method with arc length 1 was used with C3D8R linear brick elements for unstructured dog bones. For the auxetic dog bones, S4R type shell elements were used. As the structure's hinges experience the highest stress, mesh seeding was applied with curvature control to have finer meshes at those locations. A partition was also applied to the designs to improve meshing further. The dog bone was fixed in all directions (encastre) on the bottom surface, and a 1 mm (16% strain) displacement was applied to the top to mirror the experiment performed.

Table 1. Dimensions of the arrayed auxetic designs seen in Figure 1 with referred annotations, with thickness 45 µm and width *W* of 35 µm.

Auxetic	*Θ* [°]	*H* [µm]	*L* [µm]	*D* [µm]
Design 1	60	250	250	–
Design 2	$\Theta_1 = 45$ $\Theta_2 = 60$	350	160	–
Design 3	90	110	100	$D_1 = 45$ $D_2 = 270$
Design 4	75	110	110	130

3. Results and Discussion

Tensile tests were performed for both unstructured and arrayed auxetic structure dog bones, with the unstructured samples used to determine the material parameters, with the results of the tests displayed in **Figure 2**.

In Figure 2a, five cycles of the SME composition are displayed, showing no recovery of the strains applied in the first cycle as expected for SME composition alloys. Figure 2b illustrates the same experiment using the SE composition. Here, a full recovery of the superelastic strain is achieved for the investigated five cycles. The obtained experimental data are

Table 2. Superelastic material model parameters used in the simulations.

E_A [MPa]	E_M [MPa]	ν_A, ν_M	σ^S_{tL} [MPa]	σ^E_{tL} [MPa]	σ^S_{tU} [MPa]
25 000	20 000	0.3	440	560	300
σ^E_{tU} [MPa]	ε_L	σ^S_{cL} [MPa]	$(\delta\sigma/\delta T)_L$	$(\delta\sigma/\delta T)_U$	T_o [°C]
250	0.008	595	8.08	8.58	26

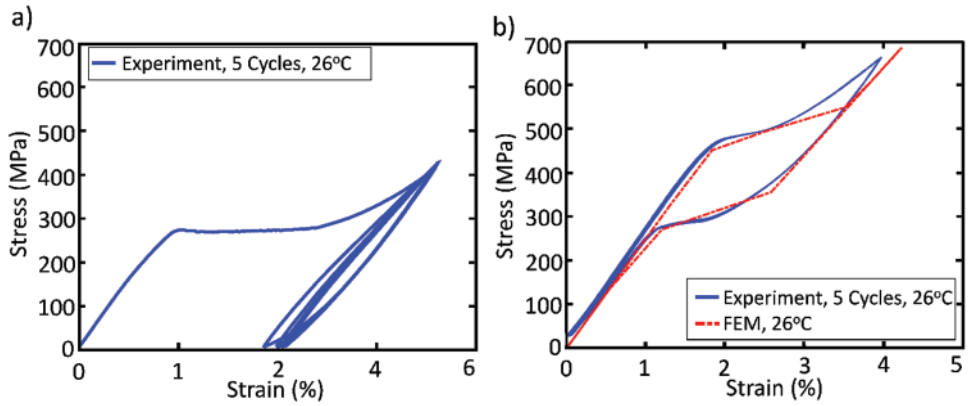

Figure 2. Five consecutive uniaxial tensile tests (blue line) were performed at 26 ± 1 °C for standard dog bone samples to characterize the shape memory and superelastic behavior of the binary NiTi material used in this study. a) The shape memory effect sample behaves as expected and shows no recoverable strain. b) The superelastic material model (red dashed line) used for the FEM simulation is consistent with the experiment of the binary SE NiTi sample.

compared with the simulation results (dashed red line). In the experimental setup, all the tensile tests are performed with 0.5 N pre-load at a temperature of 26 ± 1 °C. The simulations, however, do not contain a pre-load, which results in a slight shift of the loading curves.

A total of four designs were fabricated and investigated in this study. SEM images of the superelastic samples (**Figure 3**) are used to characterize close-up and arrayed unit cells under 0% and 12.5% strains. All unit cells show auxetic behavior apparent by the elongation in the direction of applied stress

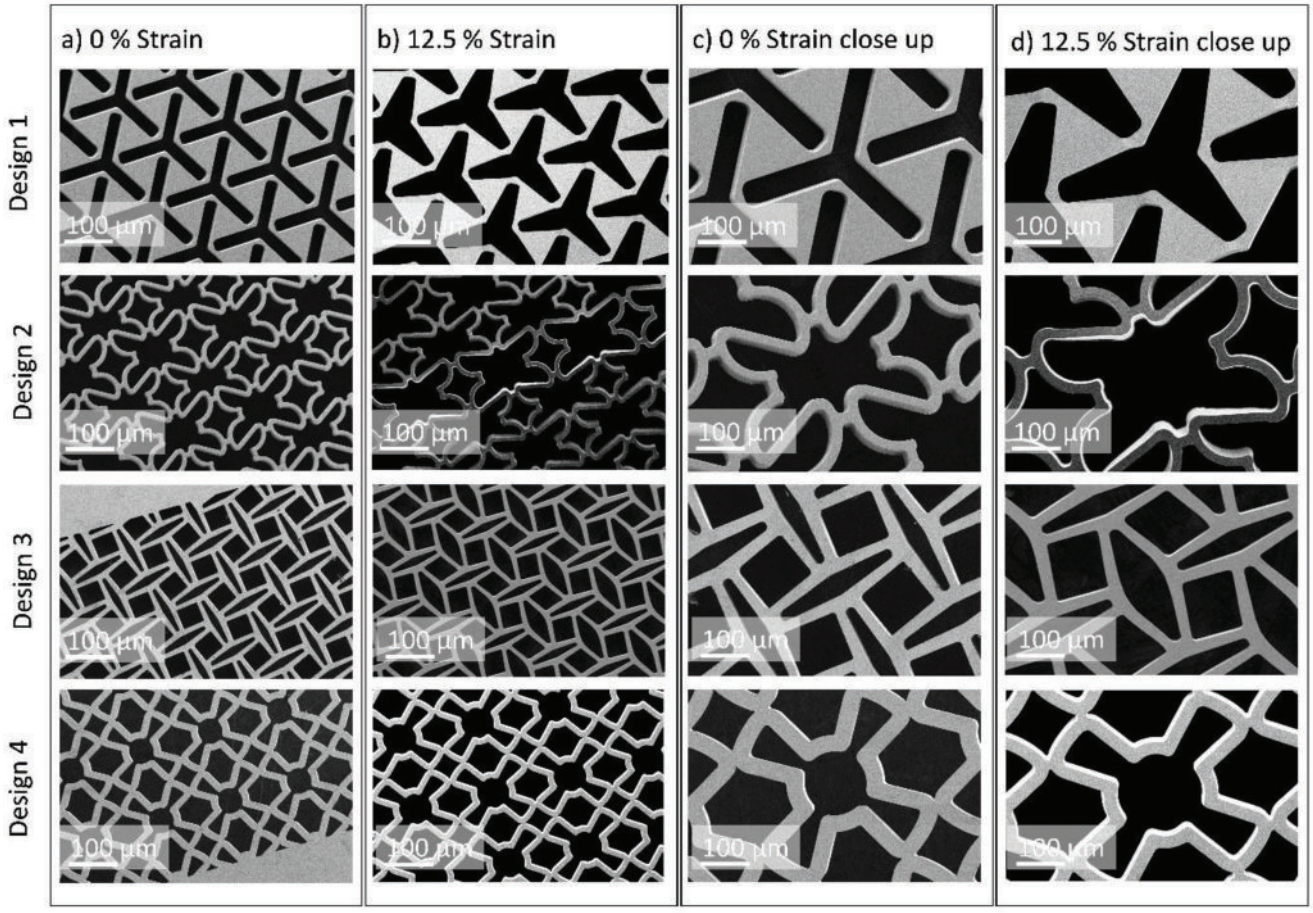

Figure 3. SEM images of auxetic arrayed structures of the different designs at a) equilibrium (0% strain) and b) applied 12.5% uniaxial strain. Magnification of a single unit cell from the array at c) equilibrium (0% strain) and d) after 12.5% uniaxial strain.

and perpendicular to it. Designs 1 and 2 show a more pronounced auxetic behavior than Designs 3 and 4 (Figure 3c,d). These close-up results show good agreement with deformation data presented in **Figure 4**a obtained by FEM simulation of the superelastic samples. All the designs have a thickness-width ratio above one to avoid the buckling region and to be in

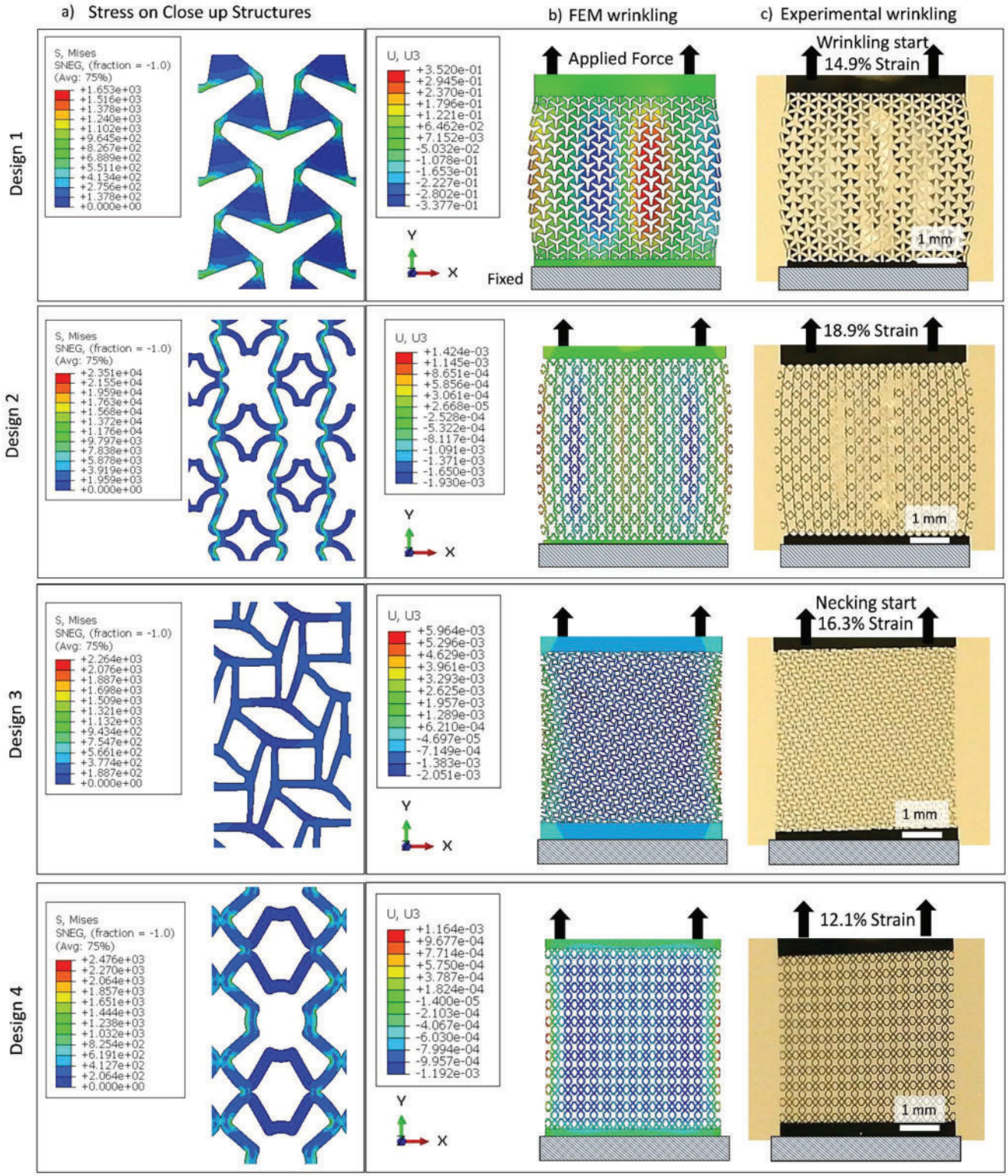

Figure 4. FEM wrinkling results of the four designs with superelastic model implemented a) a unit cell from the array displaying the von-Mises stress distribution, b) comparison between simulation and c) experiment for the samples made of superelastic material for wrinkling, U3 (z-direction) represents out-of-plane deformation compared, both simulations and experiments at 26 ± 1 °C.

the in-plane scissoring region. Design 2 in the close-up image under 12.5% showed some buckling. Furthermore, to check thickness-width effect on stretchability, Design 3 is prepared with different hinge widths with the same thickness to have a thickness-width ratio. Nonetheless, they have shown the same non-wrinkling behavior (see Figure S2, Supporting Information). For the sake of simplicity, the thickness–width effect is not further discussed in this study.

A comparison of the FEM simulation with experimental results for the arrayed designs and microscopic and macroscopic mechanical response is presented in Figure 4. These experiments and simulations were performed uniformly for the superelastic alloy SE under 16% strain to ensure being in the wrinkling regime. In the figure, the left column shows the FEM simulations of the close-up of a unit cell, colored with the von-Mises stress experienced. The middle column contains the FEM simulation of the whole structure. Here the color map displays out-of-plain deformation (U3). The right column includes the corresponding photos of the experiments. Designs 1 and 2 have a high overall negative Poisson's ratio, leading to wrinkling after critical strains, as discussed later. The corresponding Poisson's ratio values can be found in Figure 7a. The wrinkling is due to the large negative Poisson's ratio of the unit cells, which results in an expansion in the direction perpendicular to the tensile stress. Above critical stress, unit cell blocking leads to evasive movements due to buckling in the direction perpendicular to the structure plane, as in-plane deformation is prevented by already deformed unit cells. Designs 3 and 4 exhibit a Poisson's ratios close to zero, and consequently, very little stress or strain has to be compensated perpendicular to the tensile direction. Therefore, no wrinkling occurs. Video S1 (Supporting Information) shows Design 1 initially compressed goes under tensile stress and superelastic behavior after unloading till initial compressed state. This shows these structures can have cycling behavior with recovery.

Figure 5 shows the strain recovery of superelastic arrays of Design 1 with wrinkling and Design 4 without wrinkling by applying strains up to 12%. Design 2 and Design 3 show similar results under the same strain conditions to Designs 1 and 4, respectively. Thus, for simplicity, they can be found in Figure S3 (Supporting Information). Also, the occurrence of the hysteresis loop confirms the utilization of the stress-induced martensitic phase transition. The recovery of the four designs shows similar behavior. It can also be seen that residual strain remains due to remnant martensite in the material. For Design 1 and Design 4 the residual strain after the 5th cycle is 1.2% and 1.6%, respectively. However, for application requiring high number of cycles, fatigue (residual strain) could be overcome by using another type of shape memory alloy such as TiNiCu. It has been shown that SMA can withstand 10 million cycles with extremely low fatigue.[23] In Figure 5, both designs show different force values, this is due to the design of the unit cells. For example, using similar TiNi thin films, Loger et al. have shown that simple rhombic designs exhibit different hysteresis loops when unit cell orientation is changed. This leads to different stiffness of the overall design, which in turn leads to different material amount undergoing stress-induced phase transformation.[47]

Superelastic SMAs still show mechanical advantages to use as substrate compassion to conventional materials. Bossuyt et al. studied the cycling behavior of typical substrate material copper embedded in a polymer for stretchable electronics. They found that Cu leads to failure with up to 5% strains.[24]

In **Figure 6**, photos of the two designs (Design 1 and Design 4) are shown, made from the SME alloy, studied at temperatures of 26 ± 1 °C. The other designs, Design 2 and Design 3, show similar results to Designs 1 and 4, respectively. Thus, for simplicity, they can be found in Figure S4 (Supporting Information). Here, the structures in the unloaded state are in the martensite phase. For strain recovery, the specimens would have to be heated to undergo a phase transformation to austenite. From left to right, the first column shows the initial state, the second column is a snapshot just before wrinkling, the third column is an intermediate strain state within the wrinkling regime, and the fourth is the maximum strain just before structural failure. The differences in total strains can be explained by the geometrical properties of the designs. Design 1, with the largest strains, has a more compact initial state, and by expansion, it can cover large angles to be fully open up.[43] Furthermore, combining auxetics with SMAs also shows importance compared to typical metals; the higher the intrinsic strain, the larger the total strain. In Figure 6a, Design 1 shows very high strains, up to 57.4%, just before failure. SMA auxetics show high strains compared to single-layer auxetic polymer thin films are reported up to 25% strains[8] and stainless steel auxetic thin films up 18.7%[14] without recovery. The recovery of the ruptured Design 3 by

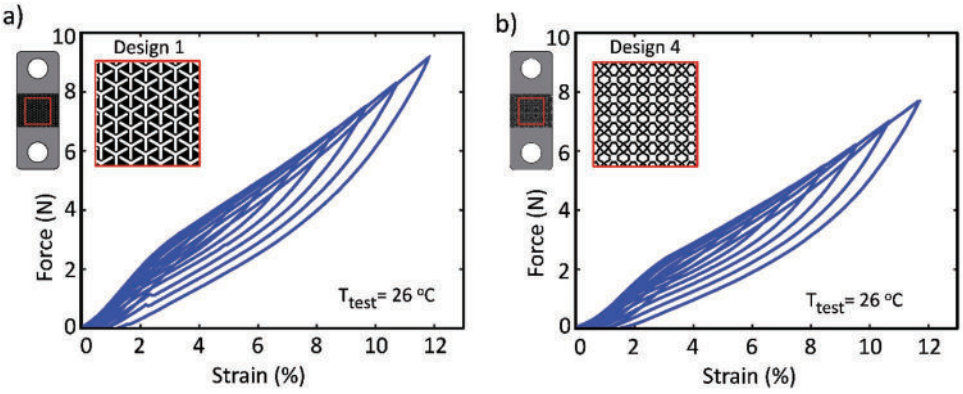

Figure 5. Hysteresis loop of auxetic arrays at 26 ± 1 °C a) Design 1 and b) Design 3. The inset shows the designs of the arrayed structures.

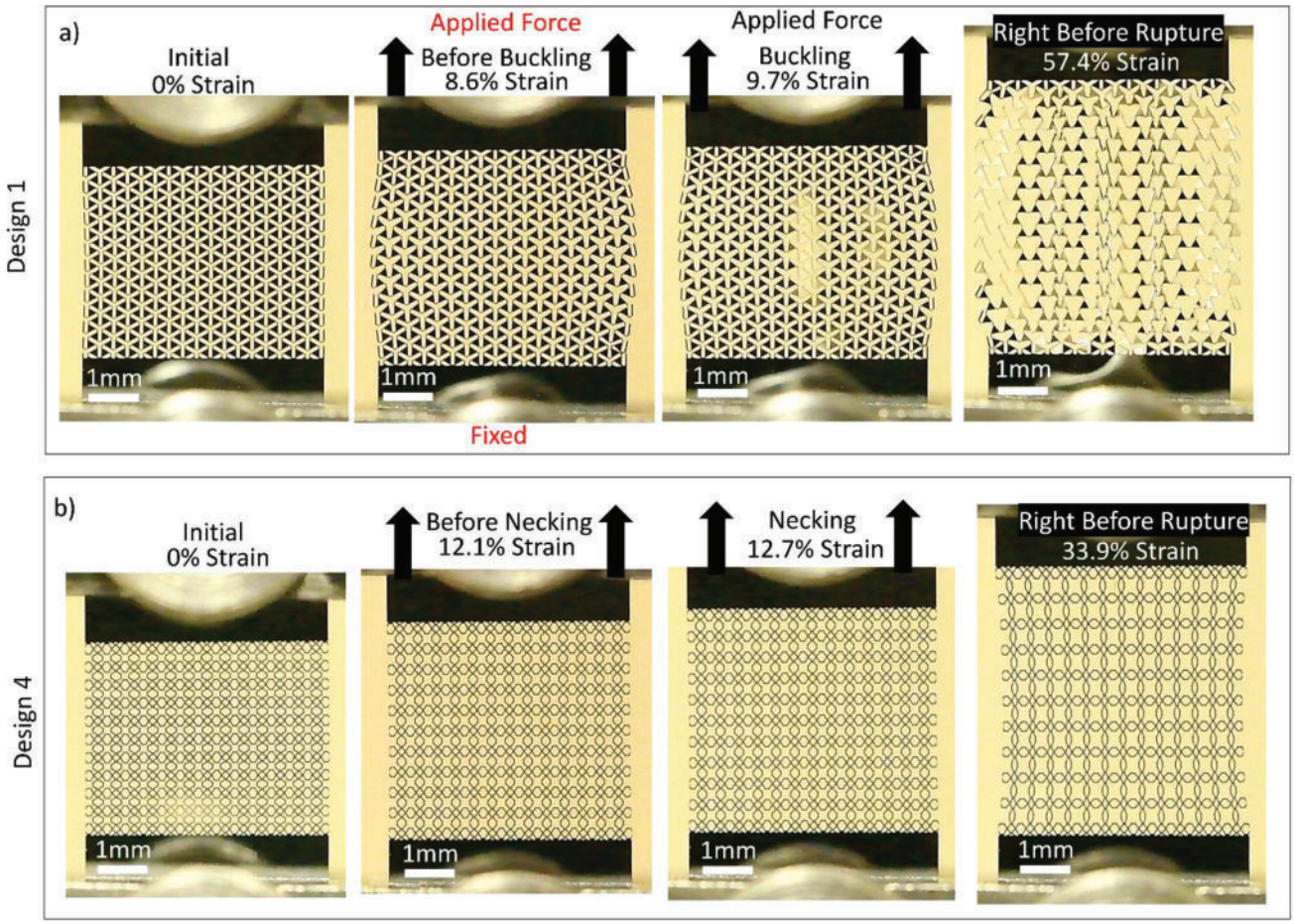

Figure 6. Two designs are shown made out of alloy SME under tensile load photos taken at 26 ± 1 °C. a) Design 1 photos left to right display initial state, right before wrinkling, wrinkling start, and before fracture, respectively and b) Design 4 display initial state, right before necking, necking start, and before fracture, respectively.

heating can be seen in Video S2 (Supporting Information). Furthermore, Designs 3 and 4, with an overall close to zero Poisson's ratio, showed strains up to 33.9%, which is higher than single-layer zero Poisson's ratio polymer thin films up to 20% without wrinkling, reported in the literature.[48]

ImageJ is used to extract the longitudinal and lateral strain values and Poisson's ratios of the experiments. Poisson's ratios are calculated from those strains. **Figure 7** displays the change in Poisson's ratio as a function of applied strain for both materials. Designs 1 and 2 show a negative Poisson ratio, while

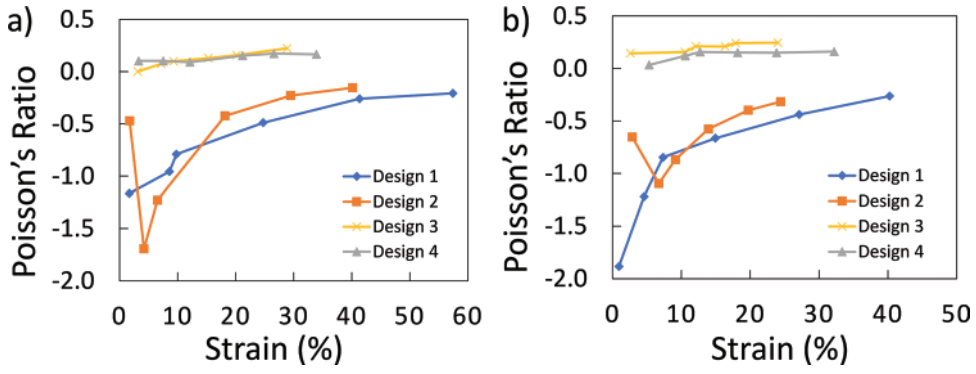

Figure 7. Poisson's ratio changes by applied strain for Designs 1–4 with obtained from the tensile testing photos analyzed using ImageJ for a) superelastic samples and b) shape memory effect samples.

Designs 3 and 4 exhibited a close to zero Poisson's ratio rather than a negative one. This can be explained by the cancellation effect seen by two competing mechanisms: the material inherently wants to exhibit conventional behavior as seen by positive Poisson's ratio materials but at the same time the auxetic unit cells expand. The interplay between these mechanisms create this apparent net zero (or close to zero) Poisson's ratio. After the design reaches certain strains, Poisson's ratio eventually and gradually increases as seen in Figure 7. This is an indication where the designs tend to show conventional behavior (i.e., necking) which leads to positive Poisson's ratio. This may occur due to higher strains on the hinges resulting in the material's deformation and buckling. This is validated by studies that have reported the change of Poisson's ratio as a function of strain.[9,49] The SME sample results, illustrated in Figure 7b, are characterized by higher intrinsic strains (see Figure 2). This leads to higher stretchability compared to superelastic material, and the results are shown in Figure 7a. This is not a general statement of whether superelastic or shape memory alloys are used. The Poisson's ratio increases with increasing strain since wrinkling occurs as instability within the structures lead to a sudden collapse in the neighboring cell after critical strains due to fixed boundary conditions caused by the tensile clamps. With further stretching, the wrinkled structures stabilize and consequently also the Poisson's ratio. This leads to a reduction in Poisson's ratio with the start of wrinkling and stabilization after certain strains. The critical strains for wrinkling for Designs 1 and 3 are 8.6% and 4.3%, respectively.

Furthermore, for both types of SMAs, length (longitudinal length see Figure 1)-to-width (lateral length see Figure 1) aspect ratio can have an effect on wrinkling formation. An increase in L/W reduces the number of wrinkles. However, this increases the amplitude of the waves. In this paper, L (5 mm)/W (4 mm) = 1.25, Zhu et al.[50] and Kumar et al.[51] showed that an aspect ratio closer to 1 can show a lower inflection point, means that they wrinkle at lower strains. In simple words, the tensile area gets close to a square $L \leq W$ than a slender rectangle $L << W$, and the wrinkling strains reduce. Our structures show wrinkling stability with having aspect ratio L (5 mm)/W (4 mm) = 1.25, close to a square. This shows that it can get stability by structuring the thin films with specific auxetic designs.

4. Conclusion

This paper investigates four different auxetic mechanisms with the miniaturization technique offered by MEMS using free-standing shape memory metallic thin films. As a shape memory alloy, TiNi binary alloy is used with two different compositions, one showing superelasticity and the other the shape memory effect. Depending on the application, the superelastic or shape memory effect could be used for full recovery by unloading or heating.

Our results show wrinkling stabilization can be achieved under very high strains, up to 33.9%, by implementing auxetics designs. Adjusting the Poisson's ratio close to zero can be achieved by compensating the necking strains with the auxetic strain in the opposite direction, thus preventing wrinkling.

For future work and design development, a finite element superelastic model can be used with the Riks method to check the stability of the design for wrinkling without the need to perform experiments. Special attention is needed to develop stable stretchable structures. However, the insights provided by the FEM results may improve thin film behavior and design for applications such as stretchable electronics, medical patches, implants, and MEMS applications.

Supporting Information

Supporting Information is available from the Wiley Online Library or from the author.

Acknowledgements

The authors want to thank the DFG via Research Training Group 2154 Materials for Brain Project number 270394294 for the funding. S.C. gratefully acknowledges support from the National Science Foundation Graduate Research Fellowship under Grant No. DGE 1840340.

Open access funding enabled and organized by Projekt DEAL.

Conflict of Interest

The authors declare no conflict of interest.

Data Availability Statement

The data that support the findings of this study are available on request from the corresponding author. The data are not publicly available due to privacy or ethical restrictions.

Keywords

auxetics, shape memory alloys, superelasticity, wrinkling stabilization

Received: November 22, 2022
Revised: January 28, 2023
Published online: March 22, 2023

[1] A. V. Mazaev, O. Ajeneza, M. V. Shitikova, in *IOP Conference Series: Materials Science and Engineering*, Institute of Physics Publishing, Moscow, Russia **2020**, p. 747.
[2] M. Konaković-Luković, J. Panetta, K. Crane, M. Pauly, *ACM Trans. Graph.* **2018**, *37*, 1.
[3] J. Zhang, G. Lu, Z. You, *Composites, Part B* **2020**, *201*, 108340.
[4] R. P. Bohara, S. Linforth, A. Ghazlan, T. Nguyen, A. Remennikov, T. Ngo, *Compos. Struct.* **2022**, *280*, 114907.
[5] A. Alderson, J. Rasburn, S. Ameer-Beg, P. G. Mullarkey, W. Perrie, K. E. Evans, *Ind. Eng. Chem. Res.* **2000**, *39*, 654.
[6] B. Jang, S. Won, J. Kim, J. Kim, M. Oh, H. J. Lee, J. H. Kim, *Adv. Funct. Mater.* **2022**, *32*, 2113299.
[7] F. Amin, M. N. Ali, U. Ansari, M. Mir, M. A. Minhas, W. Shahid, *J. Appl. Biomater. Funct. Mater.* **2015**, *13*, E127.
[8] D. Y. Fozdar, P. Soman, J. W. Lee, L. H. Han, S. Chen, *Adv. Funct. Mater.* **2011**, *21*, 2712.

[9] P. Soman, D. Y. Fozdar, J. W. Lee, A. Phadke, S. Varghese, S. Chen, *Soft Matter* **2012**, *8*, 4946.
[10] D. Photiou, S. Avraam, F. Sillani, F. Verga, O. Jay, L. Papadakis, *Appl. Sci.* **2021**, *11*, 10362.
[11] M. Panico, C. Langella, C. Santulli, *Emerg. Sci. J.* **2017**, *1*, 105.
[12] E. Khare, S. Temple, I. Tomov, F. Zhang, S. K. Smoukov, *Front. Mater.* **2018**, *5*, 45.
[13] A. Mauko, T. Fíla, J. Falta, P. Koudelka, V. Rada, M. Neuhäuserová, P. Zlámal, M. Vesenjak, O. Jiroušek, Z. Ren, *Metals* **2020**, *11*, 52.
[14] H. Lekesiz, S. K. Bhullar, A. A. Karaca, M. B. G. Jun, *Smart Mater. Struct.* **2017**, *26*, 085022.
[15] S. Jacobs, C. Coconnier, D. Dimaio, F. Scarpa, M. Toso, J. Martinez, *Smart Mater. Struct.* **2012**, *21*, 075013.
[16] H. Hassanin, A. Abena, M. A. Elsayed, K. Essa, *Micromachines* **2020**, *11*, 745.
[17] D. Kim, I. Ferretto, C. Leinenbach, W. Lee, *Adv. Mater. Interfaces* **2022**, *9*, 2200171.
[18] S. M. Curtis, D. Dengiz, L. Bumke, E. Quandt, S. M. Curtis, in *International Conference on Shape Memory and Superelastic Technologies, SMST 2022*, ASM International, San Diego, USA, **2022**, pp. 11–13.
[19] F. Amarante dos Santos, *Struct. Control Health Monit.* **2017**, *24*, e1993.
[20] K. Otsuka, X. Ren, *Prog. Mater. Sci.* **2005**, *50*, 511.
[21] J. Zhang, W. Cai, X. Ren, K. Otsuka, M. Asai, *Mater. Trans. JIM* **1999**, *40*, 1367.
[22] J. Frenzel, A. Wieczorek, I. Opahle, B. Maaß, R. Drautz, G. Eggeler, *Acta Mater.* **2015**, *90*, 213.
[23] C. Chluba, W. Ge, R. L. DeMiranda, J. Strobel, L. Kienle, E. Quandt, M. Wuttig, *Science* **2015**, *348*, 1004.
[24] F. Bossuyt, J. Guenther, T. Löher, M. Seckel, T. Sterken, J. de Vries, *Microelectron. Reliab.* **2011**, *51*, 628.
[25] J. Zhu, Q. Zeng, T. Fu, *Corros. Rev.* **2019**, *37*, 539.
[26] S. M. Curtis, J. L. Gugat, L. Bumke, D. Dengiz, L. Seigner, D. Schmadel, N. S. Lazarus, E. Quandt, *Shape Memory and Superelasticity*, ASM International, **2023**, https://doi.org/10.1007/s40830-023-00422-4.
[27] E. Cerda, K. Ravi-Chandar, L. Mahadevan, *Nature* **2002**, *419*, 579.
[28] T. Wang, Y. Yang, F. Xu, *Proc. R. Soc. A* **2022**, *478*, 20220149.
[29] Y. Su, X. Ping, K. Jun Yu, J. Woo Lee, J. A. Fan, B. Wang, M. Li, R. Li, D. V. Harburg, Y. Huang, C. Yu, S. Mao, J. Shim, Q. Yang, P.-Y. Lee, A. Armonas, K.-J. Choi, Y. Yang, U. Paik, T. Chang, T. J. Dawidczyk, Y. Huang, S. Wang, J. A. Rogers, *Adv. Mater.* **2017**, *29*, 1604989.
[30] P. Y. K. Pang, P. T. L. Chiam, Y. L. Chua, Y. K. Sin, *Eur. J. Cardio-Thoracic Surg.* **2012**, *41*, 1195.
[31] B. R. Becker, W. Jacob, S. Dolla, B. A. Fricke, *J. Med. Devices* **2007**, *1*, 47.
[32] T. Wang, Y. Yang, C. Fu, F. Liu, K. Wang, F. Xu, *J. Mech. Phys. Solids* **2020**, *134*, 103738.
[33] J. S. Plante, S. Dubowsky, *Int. J. Solids Struct.* **2006**, *43*, 7727.
[34] C. Fu, T. Wang, F. Xu, Y. Huo, M. Potier-Ferry, *J. Mech. Phys. Solids* **2019**, *124*, 446.
[35] S. J. Li, K. Wu, H. Z. Yuan, J. Y. Zhang, G. Liu, J. Sun, *Surf. Coat. Technol.* **2019**, *362*, 35.
[36] S. Yu, Y. Ni, L. He, Q. L. Ye, *ACS Appl. Mater. Interfaces* **2015**, *7*, 5160.
[37] E. A. Flores-Johnson, T. J. Rupert, K. J. Hemker, D. S. Gianola, Y. Gan, *Extreme Mech. Lett.* **2015**, *4*, 175.
[38] A. Bonfanti, A. Bhaskar, *Extreme Mech. Lett.* **2020**, *33*, 100556.
[39] C. Chluba, K. Siemsen, C. Bechtold, C. Zamponi, C. Selhuber-Unkel, E. Quandt, R. Lima de Miranda, *Biosens. Bioelectron.* **2020**, *153*, 112034.
[40] V. Röbisch, A. Piorra, R. Lima De Miranda, E. Quandt, D. Meyners, *AIP Adv.* **2018**, *8*, 125320.
[41] S. M. Curtis, N. Wolff, D. Dengiz, H. Lewitz, J. Jetter, L. Bumke, P. Hayes, E. Yarar, L. Thormählen, L. Kienle, D. Meyners, E. Quandt, *J. Mater. Res.* **2020**, *35*, 1298.
[42] C. Bechtold, R. Lima de Miranda, E. Quandt, *Shape Mem. Superelasticity* **2015**, *1*, 286.
[43] J. N. Grima, K. E. Evans, *J. Mater. Sci.* **2006**, *41*, 3193.
[44] K. Meena, S. Singamneni, *Mater. Des.* **2019**, *173*, 107779.
[45] P. Eghbali, D. Younesian, A. Moayedizadeh, M. Ranjbar, *Sci. Rep.* **2020**, *10*, 16338.
[46] P. Velvaluri, M. S. Pravdivtseva, R. Lima de Miranda, J. B. Hövener, O. Jansen, E. Quandt, *Shape Mem. Superelasticity* **2019**, *5*, 195.
[47] K. Loger, A. Engel, J. Haupt, Q. Li, R. Lima De Miranda, E. Quandt, G. Lutter, C. Selhuber-Unkel, *Mater. Sci. Eng., C* **2016**, *59*, 611.
[48] P. Soman, D. Y. Fozdar, J. W. Lee, A. Phadke, S. Varghese, S. Chen, *Soft Matter* **2012**, *8*, 4946.
[49] P. D. Dubrovski, N. Novak, M. Borovinšek, M. Vesenjak, Z. Ren, *Polymers* **2019**, *11*, 1040.
[50] J. Zhu, X. Zhang, T. Wierzbicki, *Int. J. Solids Struct.* **2018**, *139–140*, 238.
[51] S. Kumar, S. Upadhyay, A. C. Mathur, *J. Vibration Anal.* **2015**, *3*, 17.